

The distance to the Orion Nebula Cluster

R.D. Jeffries

Astrophysics Group, School of Physical and Geographical Sciences, Keele University, Keele, Staffordshire ST5 5BG

Submitted December 5 2006

ABSTRACT

The distance to the Orion Nebula Cluster (ONC) is estimated using the rotational properties of its low-mass pre main-sequence (PMS) stars. Rotation periods, projected equatorial velocities and distance-dependent radius estimates are used to form an observational $\sin i$ distribution (where i is the axial inclination), which is modelled to obtain the distance estimate. A distance of 440 ± 34 pc is found from a sample of 74 PMS stars with spectral types between G6 and M2, but this falls to 392 ± 32 pc when PMS stars with accretion discs are excluded on the basis of their near-infrared excess. Since the radii of accreting stars are more uncertain and probably systematically underestimated, then this closer distance is preferred. The quoted uncertainties include statistical errors and uncertainties due to a number of systematic effects including binarity and inclination bias. This method is geometric and independent of stellar evolution models, though does rely on the assumption of random axial orientations and the Cohen & Kuhi (1979) effective temperature scale for PMS stars. The new distance is consistent with, although lower and more precise, than most previous ONC distance estimates. A closer ONC distance implies smaller luminosities and an increased age based on the positions of PMS stars in the Hertzsprung-Russell diagram.

Key words: stars: formation – stars: distances – methods: statistical – open clusters and associations: M42

1 INTRODUCTION

The Orion Nebula cluster (ONC) is among the best studied star forming regions. It is perhaps the premier cluster for investigating star formation and early stellar evolution because it is relatively nearby, very young (< 2 Myr) and contains a large population of stars and brown dwarfs covering the entire (sub)stellar mass spectrum ($0.01 < M/M_{\odot} < 30$ – see Hillenbrand 1997; Slesnick, Hillenbrand & Carpenter 2004). The ONC lies just in front of the dense OMC-1 molecular cloud, so background contamination of cluster candidates is small and proper motion studies have successfully ascribed membership to almost 1000 stars (Jones & Walker 1988). The ONC is a focus for understanding the initial stellar mass function, the evolution of circumstellar discs, early stellar angular momentum loss, the influence of high mass stars on lower mass siblings and their discs, X-ray activity in young stars, the history of star formation and the formation of star clusters in general (e.g. see Hillenbrand et al. 1998; O'Dell 1998; Lada et al. 2000; Muench et al. 2002; Herbst et al. 2002; Preibisch et al. 2005; Huff & Stahler 2006; Shuping et al. 2006 among many others).

The distance to the ONC is quite poorly constrained – anywhere between 350 pc and 550 pc, with a most likely range of 400–500 pc depending on which techniques are considered most reliable (see section 2). The distance is an im-

portant parameter in determining absolute dimensions, velocities and mass loss rates in the cluster as well as for estimating stellar luminosities and hence masses and ages from evolutionary tracks.

In this paper the distance to the ONC is determined using the rotational properties of pre main-sequence (PMS) stars (axial rotation periods P , and projected equatorial velocities $v \sin i$, where i is the inclination angle of the spin axis to the line of sight), together with estimates of stellar radii. From these, the observed distribution of $\sin i$ can be compared to a model that assumes random spin axis orientation and appropriate contributions from uncertainties in the observational parameters. Because the estimated stellar radii scale linearly with distance, the distance can be treated as a free parameter in the model to optimise the match between observed and predicted distributions.

This technique was developed initially by Hendry, O'Dell & Collier Cameron (1993) and used to derive a distance of 132 ± 10 pc to the Pleiades, which compares well with the currently accepted Pleiades distance from numerous other techniques (O'Dell, Hendry & Collier Cameron 1994). Preibisch & Smith (1997) used a variant of the method to find a distance to T-Tauri stars in the Taurus star forming region. Again, the distance they found of 152 ± 10 pc

arXiv:astro-ph/0701186v1 8 Jan 2007

now compares well with distances from Hipparcos parallaxes (Bertout, Robichon & Arenou 1999).

In section 2 previous estimates of the distance to the ONC are reviewed. The database of ONC rotation measurements that were used for this work is discussed in section 3. The modelling technique is described in section 4, which also discusses systematic effects that must be taken into account. The results are presented in section 5 and their robustness against variations in the model parameters and assumptions is tested. Conclusions and a brief discussion are presented in section 6.

2 PREVIOUS DISTANCE ESTIMATES TO THE ONC

Most previous distance estimates were based on fits to the upper main sequence of the ONC in the Hertzsprung-Russell (HR) diagram and hampered by colour excesses, variable extinction, the nebular background and uncertain binarity. Walker (1969) found a distance modulus of 8.37 ± 0.05 (472 pc) from *UBV* photometry of relatively unobscured stars in the outskirts of the ONC. However, Penston, Hunter & O'Neill (1975) obtained optical and near infrared photometry in a 40 arcminute box around the ONC, determining distance moduli of 8.1 ± 0.1 (417 pc) from the *V, B - V* colour magnitude diagram (CMD), and only 7.7 (347 pc) from the *V, V - I* CMD. More recent estimates used the large *UBVubvy* dataset of Warren & Hesser (1978). These authors found a distance modulus of 8.42 ± 0.24 (483 pc) for the Orion OB1d1 subregion, which is a ~ 30 arcminute diameter box around the ONC, but excluding the central few arcminutes around the central Trapezium cluster of high-mass stars. Anthony-Twarog (1982) used the same data with somewhat different calibrations to obtain a distance modulus of 8.19 ± 0.10 (435 pc). Breger, Gehrz & Hackwell (1981) used infrared and broad band polarisation measurements to exclude objects that showed abnormal reddening or evidence for circumstellar material and found that the remaining objects have an average distance modulus of 8.0 ± 0.1 (400 pc) in the *V, B - V* CMD. The significant discrepancy between for example Walker's (1967) and Breger et al.'s (1981) distance estimates points to the fact that there may be substantial additional systematic uncertainties present in these HR diagram-based results.

Unfortunately, no light is shed on these varying distance estimates by other independent techniques. Only one star in the ONC has a direct parallax measurement from Hipparcos, yielding a distance of 361^{+168}_{-87} pc (Bertout et al. 1999). A more indirect but frequently cited constraint was provided by Genzel et al. (1981). Using an expanding cluster parallax method they analysed the proper motions and radial velocities of H₂O masers in the Kleinmann-Low nebula (part of OMC-1), thought to be just behind the ONC, and obtained a distance of 480 ± 80 pc. Finally, Stassun et al. (2004) found an eclipsing binary just 20 arcminutes south of the Trapezium stars. They determined absolute radii and effective temperatures for the components and hence estimated a distance of 419 ± 21 pc from the system photometry. However, Stassun et al. suggest that this binary system might be foreground to the ONC because at that distance

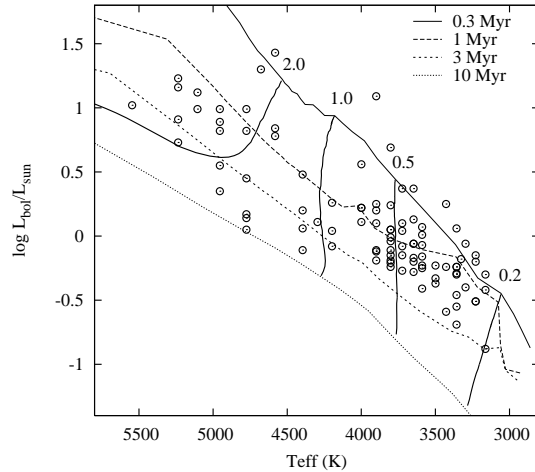


Figure 1. A Hertzsprung-Russell diagram for the 95 stars of the ONC rotation sample (see text) assuming an ONC distance of 470 pc. Model isochrones and evolutionary tracks from Siess et al. (2000) are shown. Masses are labelled in solar units.

the object appears older by a few Myr than the bulk of the ONC population.

3 CONSTRUCTION OF THE DATABASE

The observed $\sin i$ distribution in the ONC was investigated using a database founded on the catalogue of ONC axial rotation periods constructed by Herbst et al. (2002). This catalogue also includes rotation periods measured by Stassun et al. (1999) and Herbst et al. (2000). From this, all objects were selected that had an entry in the Jones & Walker (1988) catalogue of proper motions within 15 arcminutes of the ONC centre and a spectral type, effective temperature (T_{eff}), luminosity (L) and radius (R) estimate listed by Hillenbrand (1997). The L and R estimates in Hillenbrand (1997) assume an ONC distance of 470 pc. Almost all of these stars also have a measurement of their $I - K$ excess – i.e. the excess colour over that expected from the photosphere of a “normal” star of similar spectral type. Measurements of the equivalent width (EW) of the Ca II 8542Å line, which is also diagnostic of accretion, are also available for most of the sample from Hillenbrand et al. (1998).

From this subset, $v \sin i$ measurements were found in the catalogues of Rhode et al. (2001) and Sicilia-Aguilar et al. (2005). The latter work was performed at a higher resolving power (34 000 versus 21 500) and so values from Sicilia-Aguilar et al. were preferred for $v \sin i$ values less than 20 km s^{-1} . For higher velocities the measurement with the best quoted fractional precision was chosen. Objects with only upper limits to their $v \sin i$ were excluded. Three objects (JW 192, JW 381 and JW 710) where Herbst et al. (2002) state that the measured periods are highly uncertain were also excluded.

3.1 Measurement uncertainties

The periods measured for low-mass PMS stars are generally very precise and accurate, relying on the co-rotation

Table 1. Database of objects considered in this work. The full table is available in electronic form and contains 95 rows. A sample is given here to illustrate its content. Column 1 gives the identifying number from Jones & Walker (1988); columns 2 and 3 list the spectral type and T_{eff} from Hillenbrand (1997); columns 4, 5 and 6 list the $v \sin i$, its uncertainty and the source of the rotational velocity membership (1 – Rhode et al. [2001], 2 – Sicilia-Aguilar et al. [2005]); column 7 lists the rotational period as given by Herbst et al. (2002); columns 8, 9 and 10 list the log bolometric luminosity (in solar units), stellar radius (assuming a cluster distance of 470 pc) and $\Delta(I - K)$ from Hillenbrand (1997); column 11 gives the equivalent width of the 8542Å CaII line from Hillenbrand et al. (1998) [negative indicates an emission line]; column 12 lists the derived $\sin i$.

JW	SpT	T_{eff} (K)	$v \sin i$ (km s ⁻¹)	$\Delta v \sin i$ (km s ⁻¹)	Source	P (d)	$\log L/L_{\odot}$	R/R_{\odot}	$\Delta(I - K)$ (mag)	EW[Ca] (Å)	$\sin i$
3	K8	3801.8	29.8	4.5	1	3.43	0.24	3.036	0.55	2.0	0.665
17	M4	3228.4	19.9	3.9	1	3.14	-0.20	2.537	0.10	0.8	0.486
20	M3.5	3296.0	70.3	11.6	1	0.67	-0.40	1.933	0.10	0.7	0.481
25	M4.5	3162.2	18.0	4.0	1	2.28	-0.88	1.209	0.52	0.0	0.671

of magnetic inhomogeneities (starspots) in the photosphere. Providing a sufficient time baseline and sampling frequency are obtained, period precisions of better than 1 per cent are usually achieved. Studies of objects with periods measured at more than one epoch suggest that $\simeq 90$ per cent of period measurements have at least this level of precision (Herbst et al. 2002). About 10 per cent of period measurements can be catastrophically incorrect. The periods could be too short by a factor of two if more than one spotted region on a star leads to a “double-humped” light curve that is interpreted incorrectly. Alternatively, the measured period can be *much* longer than the true periods because of aliasing with the $\simeq 1$ day sampling interval that is present in almost all datasets (see discussion in Herbst et al. 2002). Many of these incorrect periods have already been weeded out by Herbst et al. (2002) and others are suspected (e.g. the three stars excluded in the previous subsection), but it is possible that a small fraction remain. For now an uncertainty of 1 per cent on all the period measurements is assumed.

The resolution of the rotational velocity studies limits the $v \sin i$ measurements to values of more than 11 km s^{-1} and about 5 km s^{-1} from Rhode et al. (2001) and Sicilia-Aguilar et al. (2005) respectively. Above these limits the fractional precision of the $v \sin i$ measurements are of order 10 per cent, though vary from object-to-object. Rhode et al. (2001) discuss how problems in calibrating the intrinsic resolution of fibre spectrographs can lead to problematic and possibly incorrect values for $v \sin i$ when rotational broadening is close to the detection threshold. Rhode et al. suggest using $v \sin i = 13.6 \text{ km s}^{-1}$ as a more plausible detection threshold for their data, and that is what is used here. With similar reasoning only values of $v \sin i \geq 10 \text{ km s}^{-1}$ are used from the work of Sicilia-Aguilar et al. (2005). The sample is also filtered of poor quality data with a fractional $v \sin i$ uncertainty greater than 25 per cent to prevent unnecessarily broadening the observed $\sin i$ distribution.

Stellar radii are estimated from combining L and T_{eff} (Hillenbrand 1997). L comes from extinction-corrected I -band magnitudes and bolometric corrections, and assumes a distance to the ONC of 470 pc. T_{eff} values are estimated from the relationship between spectral type and T_{eff} (with some small modifications) proposed by Cohen & Kuhi (1979). Hillenbrand (1997) estimates that L is uncertain by about 0.2 dex due to variability and uncertainties in extinction. Random errors in spectral types lead to uncertainties of about 0.02 dex in the T_{eff} values. As $R \propto L^{-1/2} T_{\text{eff}}^2$, the

random errors in R are about 0.11 dex. It is fair to say that this uncertainty is itself uncertain, and so values between 0.07 dex and 0.15 dex are tested in the modelling. Hillenbrand (1997) also had concerns that because of difficulties in assigning an extinction value, the L and hence R of accreting classical T-Tauri stars (CTTS) would be *underestimated*. As the rotational database contains information on the $I - K$ excess and EW[Ca], both of which are diagnostic of strong accretion, such stars can be optionally excluded.

The final database contains 95 objects with both adequate P and $v \sin i$ measurements and estimates of L , T_{eff} and R . These objects are listed in Table 1 (available in electronic form only) and the HR diagram is compared with the stellar evolutionary models of Siess, Dufour & Forestini in Fig. 1 (2000 – the variant with a metallicity of 0.02 and no convective overshoot).

3.2 Selection effects and biases

The database is subject to a number of selection effects and biases (see also the discussion in Herbst & Mundt 2005). There is a bias against the inclusion of CTTS and in favour of weak-lined T-Tauri stars (WTTS). This is because CTTS often show accretion-related, non-periodic variability which masks the true rotation period of the star. There is also a bias towards objects with shorter rotation periods simply because these are easier to measure from datasets with a limited time span. Neither of these selection effects will bias the observed $\sin i$ distribution unless CTTS and more slowly spinning stars have non-random spin-axis orientation.

Of more concern is the observational bias against slow rotators and objects with small $\sin i$ because of the limited sensitivity of the $v \sin i$ measurements. In principle this can be accounted for in our modelling by putting a $v \sin i$ cut-off in the model. This threshold imposes a smooth roll-off in the values of $\sin i$ that are capable of detection. The exact shape of the roll-off depends on the distribution of true equatorial velocities (see section 4.2).

A further consideration is the bias away from low inclination systems due either to the lack of visibility of starspots at equatorial latitudes caused by limb darkening, or to the reduced amplitude of spot modulation caused by starspots at higher latitudes (see discussion in O’Dell & Hendry 1994). The actual latitude distribution of spots on very young stars is still debatable. There have been theoretical predictions of polar concentrations for spots on rapidly rotating stars with

deep convection zones (e.g. Schüssler et al. 1996). However, Granzer et al. (2000) predict spots over a wide range of latitude for fast-rotating T-Tauri stars, with an equatorial concentration in slower rotators. The evidence from Doppler imaging of spots on very young T-Tauri stars is mixed. Some show spot activity at low latitudes, some at high latitudes and other have spots at all latitudes (see Joncour, Bertout & Bouvier 1994; Johns-Krull & Hatzes 1997; Neuhäuser et al. 1998). For now I make the assumption that there is some inclination i_{th} , below which starspot modulation is never seen (see also O'Dell et al. 1994). This threshold is allowed to vary over some plausible range or can be tuned to give the best fit to the lower end of the observed $\sin i$ distribution.

4 MODELLING THE OBSERVED INCLINATION DISTRIBUTION

4.1 The general approach

The observational estimates of $\sin i$ for each star are given by

$$(\sin i)_{\text{obs}} = \left(\frac{k}{2\pi} \right) \frac{P_{\text{obs}} (v \sin i)_{\text{obs}}}{R_{\text{obs}}}, \quad (1)$$

where P_{obs} is the observed period, $(v \sin i)_{\text{obs}}$ is the observed projected equatorial velocity, R_{obs} is the estimate of the stellar radius based on a distance to the ONC of 470 pc, and k is a constant which depends on the units used for the various quantities. The aim is to model the distribution of $(\sin i)_{\text{obs}}$ with a Monte Carlo simulation. To that end I define

$$k = 2\pi \frac{R_{\text{true}}}{P_{\text{true}} v_{\text{true}}} \quad (2)$$

where the subscript “true” indicates the actual values of these three parameters in the absence of measurement uncertainties and other systematic effects (see below). I assume that P_{obs} is related to P_{true} by

$$P_{\text{obs}} = P_{\text{true}} (1 + \delta_P U), \quad (3)$$

where δ_P is the fractional uncertainty in the period and U is a random number drawn from a Gaussian distribution with a mean of zero and unit standard deviation. Similarly,

$$(v \sin i)_{\text{obs}} = v_{\text{true}} \sin i (1 + \delta_v U) \quad (4)$$

where $\sin i$ is drawn randomly assuming that $\cos i$ is distributed uniformly between 0 and 1 (i.e. random orientation of the spin axes) and δ_v is the fractional uncertainty in the $v \sin i$ measurements. The true velocity and $\sin i$ are split into separate factors because the effect of an observational lower limit to $v \sin i$ can only be modelled properly if a distribution of v_{true} is initially specified. For instance a star with $v_{\text{true}} = 50 \text{ km s}^{-1}$ cannot be in the Rhode et al. (2001) observational sample unless $\sin i > 13.6/50$, but clearly this threshold changes with v_{true} (see section 4.2).

There is a similar expression relating R_{obs} and R_{true} but this must also take into account that the true distance, D , which is assumed common to all stars in the sample, may differ from the 470 pc assumed by Hillenbrand (1997). In addition a term must be included that admits the possibility that a given star could be an unresolved binary system. In which case, L is the sum of two components and R_{true} could be smaller than R_{obs} by a factor, $1 \leq b \leq \sqrt{2}$, for binary mass ratios $0 \leq q \leq 1$. In this case

$$R_{\text{obs}} = R_{\text{true}} \left(\frac{470 \text{ pc}}{D} \right) b(q) 10^{\delta_{\log R} U}, \quad (5)$$

where $\delta_{\log R}$ is the uncertainty (in dex) of the logarithmic radius estimate (see section 3.1).

Hence, combining equations 1–5 the model for $(\sin i)_{\text{obs}}$ can be expressed as

$$(\sin i)_{\text{obs}} = \left[\frac{D}{470 \text{ pc}} \right] \left[\frac{(1 + \delta_P U_1)(1 + \delta_v U_2)}{b(q) 10^{\delta_{\log R} U_3}} \right] \sin i, \quad (6)$$

where U_1, U_2, U_3 indicate that these are three different random numbers taken from a unit Gaussian distribution.

To estimate the distance to the cluster I adopt the simplest, unbiased approach suggested by Hendry et al. (1993). If equation 6 is re-expressed as

$$(\sin i)_{\text{obs}} = \left[\frac{D}{470 \text{ pc}} \right] \alpha, \quad (7)$$

then taking the average over all the stars in the sample and the average over all the trials in a model Monte-Carlo simulation, the best estimate for the distance to the cluster is

$$D = 470 \left(\frac{\langle (\sin i)_{\text{obs}} \rangle}{\langle \alpha \rangle} \right) \text{ pc}. \quad (8)$$

4.2 The true equatorial velocity distribution

The model distribution for v_{true} has some influence on the derived cluster distance. The reason is that the lower threshold for $v \sin i$ measurements leads to a higher threshold in $(\sin i)_{\text{obs}}$ for lower values of v_{true} . To obtain a good model for the distribution of $(\sin i)_{\text{obs}}$ requires a reasonable description of the distribution of v_{true} . An incorrect v_{true} distribution leads to a systematic error in the distance estimate.

With the size of sample considered here this error is not entirely negligible compared with the statistical uncertainties in D (see section 5.2). Fortunately we can check that the assumed v_{true} distribution is reasonable by comparing the modelled distribution of $v \sin i$ from equation 4 (after uncertainties and selection thresholds have been applied) with that seen in the data. For instance a flat v_{true} distribution would not explain the observed $v \sin i$ distribution in the ONC (see section 5.2).

4.3 The binary correction factor

Unresolved binary systems will have systematically overestimated L , overestimated R and hence underestimated $\sin i$. A neglect of this effect would lead to an underestimated distance in equation 8. In older clusters where stars have reached the ZAMS, unresolved binaries with $q \gtrsim 0.5$ are easily detected as they lie significantly above the cluster single stars locus in the HR diagram. This becomes impractical in young clusters like the ONC where there may be an age spread that is a significant fraction of the mean age, and where differential extinction and variability cause significant spreads in any CMD.

I have calculated a correction to R that should be applied to an unresolved binary system of total luminosity L and mass ratio q . The calculation uses a model of L versus T_{eff} calculated at a range of masses. For this paper I have used the models of Siess et al. (2000) and Baraffe et al. (2002

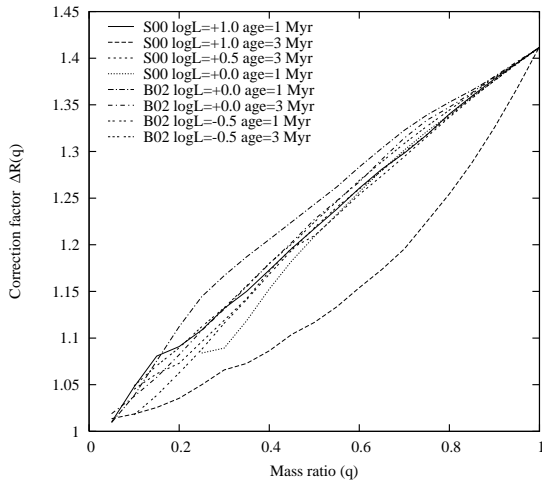


Figure 2. The multiplicative binary correction factor as a function of mass ratio for ages of 1 Myr or 3 Myr, for $-0.5 < \log(L/L_{\odot}) < 1.0$ and for two different evolutionary models (Siess et al. 2000 – S00 and Baraffe et al. 2002 – B02).

– the variant with a mixing length equal to the pressure scale height). For an assumed age and L , an initial guess (an upper limit) for m_1 is taken straight from the isochrone and an initial guess for m_2 is qm_1 . The value of m_1 is iteratively reduced until the total luminosity of the two components equals L . At this point the actual T_{eff} of the primary and secondary can be calculated as well as a flux-averaged T_{eff} that is assumed to correspond to the observed spectral type. The multiplicative overestimate of the radius is given by

$$\Delta R(q) = \left(\frac{L}{L_1}\right)^{1/2} \left(\frac{T_{\text{eff},1}}{T_{\text{eff}}}\right)^2 \quad (9)$$

In Fig. 2 I show $\Delta R(q)$ for $-0.5 < \log L/L_{\odot} < 1$ and for ages of 1 or 3 Myr that cover the majority of stars in the ONC rotation sample. At low luminosities the Baraffe et al. (2002) models are used because the Siess et al. (2000) models do not extend to low masses ($M < 0.1 M_{\odot}$), on the other hand the Baraffe et al. models do not extend to high luminosities as they are limited to masses less than $1.4 M_{\odot}$. At luminosities where the models overlap there is good agreement. These curves demonstrate that $\Delta R(q)$ is quite insensitive to changes in age, but does behave differently for older stars with high luminosity. This is caused by a sharply changing slope in the luminosity-mass relationship as stars develop a radiative core. This occurs at about $10 L_{\odot}$ at 3 Myr, but at $30 L_{\odot}$ for ages of ≤ 1 Myr. This boundary more-or-less coincides with the envelope of the sample stars considered here (see Fig. 1) and so a single $\Delta R(q)$ curve was adopted that is representative for most of the sample (the Siess et al. model with $\log L/L_{\odot} = 0.5$ at 3 Myr), which is given the label “r1” in section 5.3. To check the sensitivity of the results to this assumption the most deviant $\Delta R(q)$ curve in Fig. 2 (the Siess et al. model with $\log L/L_{\odot} = 1.0$ and at 3 Myr) is also tested in section 5.3 and given the label “r2”. The difference in derived distance between using models r1 and r2 turns out to be small (2 per cent), but the neglect of binaries altogether would lead to a distance underestimate of $\simeq 10$ per cent.

The relationship between $\Delta R(q)$ and $b(q)$ in equation 6

is set by assuming that a fraction f of star-systems are binaries, with q drawn randomly from a defined distribution. The appropriate value of f and the q distribution can be inferred from observational studies of the ONC.

Using different high spatial resolution surveys Prosser et al. (1994), Padgett, Strom & Ghez (1997), Petr et al. (1998), Simon, Close & Beck (1999) and Köhler et al. (2006) have concluded that the binary frequency in the range 100–1000 au is similar to that of field stars and probably declines towards lower masses in a similar way. Details for closer binary systems are yet to be published, but preliminary results suggest that the close binary frequency is also similar to that of field stars (Stassun & Mathieu 2006).

I make the assumption that binary properties in the ONC are similar to that of the field. Duquennoy & Mayor (1991) show that the overall binary frequency for solar-mass stars is 57 per cent and at distances of ~ 450 pc, the vast majority of these would be unresolved binaries in the ONC sample. The binary frequency declines towards 30–40 per cent in M dwarfs with $0.3\text{--}0.5 M_{\odot}$ (Fischer & Marcy 1992). The mass ratio distribution appears reasonably uniform, at least over the range $0.5 < q \leq 1$ that is most important for the phenomena considered here. The stars in our rotational sample cover a mass range of $0.2 < M/M_{\odot} < 2.5$ according to the PMS tracks of Siess et al. (2000; see Fig. 1). Rather than complicate things further, the binary frequency in the ONC is assumed to be 50 per cent, mass-independent and q is given a uniform distribution. The sensitivity of the results to these assumptions is tested by allowing the binary frequency to vary by ± 20 per cent in the simulations (see section 5.3).

It is worth stressing that one could just use an average value of $b(q)$ as a multiplicative correction factor to the distance estimate in equation 8. However, I calculate individual b values for each star in the Monte Carlo simulations because binarity introduces an extra spread in the model α distribution which should be taken into account when deciding whether the model is a reasonable fit to the data and, for instance, in deciding on an appropriate value for i_{th} (see section 3.2).

As a final remark on binary systems, I note that the $v \sin i$ measurements of very short period (less than a few days) binaries could be artificially increased by orbital motion because of the lengthy exposure times used to obtain the spectra (up to a few hours for the Rhode et al. [2001] measurements). This would increase $(\sin i)_{\text{obs}}$ for the affected objects, leading to a distance overestimate. I have neglected this possibility in the modelling, but as only a very small minority of binary systems are likely to have such short periods and be observed at unfavourable phases, this seems reasonable.

4.4 Recap of assumptions and the step-by-step method

Having described the general methods I use to calculate a model $(\sin i)_{\text{obs}}$ distribution, the following summarises the specific assumptions and steps in the modelling process.

(i) Choose the sample. Stars are selected from the rotation sample on the basis of having a minimum observed projected equatorial velocity ($v \sin i$)_{obs} (13.6 km s^{-1} and

10 km s⁻¹ for the Rhode et al. [2001] and Sicilia-Aguilar [2005] observations respectively – see section 3.1) and can be further restricted to a range of temperature and whether they show signs of accretion or not (see section 5.1).

(ii) A model is chosen for the true equatorial velocity (v_{true}) distribution. Then, assuming that the rotation axes are randomly orientated, a set (typically 10^4 trials per object in the sample) of model $v \sin i$ values are randomly generated and perturbed according to equation 4 using the fractional uncertainties in $(v \sin i)_{\text{obs}}$ as the δ_v values. The model v_{true} distribution is adjusted until a satisfactory match to the $(v \sin i)_{\text{obs}}$ distribution is indicated by a Kolmogorov-Smirnov (K-S) test between the observed and modelled cumulative distribution functions (CDFs).

(iii) The trial values of $\sin i$ are used to calculate the α values in equation 7 using δ_v , fractional errors in the period $\delta_p = 0.01$, and assuming a suitable value for the fractional error in the log stellar radius ($\delta_{\log R}$). A fraction f of the trials are randomly assigned a binary status and the appropriate correction factor to the observed radius, $b(q)$, is applied assuming that the binary mass ratio (q) is uniformly distributed.

(iv) The results of the trials pass through a filter which only allows those trials to proceed which have $v \sin i$ greater than the observational thresholds and axial inclinations greater than a user-defined threshold, i_{th} .

(v) At this stage the average value of $(\sin i)_{\text{obs}}$ is divided by the average value of α in order to find D (equation 8). At the same time a K-S test is made between the CDFs of $\alpha(D/470)$ and $(\sin i)_{\text{obs}}$. This is used to decide whether the model is a reasonable description of the data (the sample is too small to consider χ^2 tests).

(vi) Statistical uncertainties in the results are estimated by generating many fake datasets of the appropriate size. The $(\sin i)_{\text{obs}}$ values are drawn randomly using equation 7 at the estimated distance and these are modelled in the same way as the data. The standard deviation of the distance estimates is used as a statistical uncertainty.

(vii) The sensitivity of the results to the model assumptions and parameters are tested using different subsamples of data (e.g. with or without signs of accretion), different values of i_{th} , f , $\delta_{\log R}$ or different models for $\Delta R(q)$ and the v_{true} distribution (see section 5.3).

5 RESULTS

5.1 The observed $\sin i$ values

In Fig. 3 $(\sin i)_{\text{obs}}$ versus T_{eff} is plotted for the sample. The data have been distinguished on the basis of whether their near infrared excesses, $\Delta(I - K)$, are larger or smaller than 0.3. This division approximately separates stars with and without active accretion and thus the two subsets are labelled as CTTS and WTTS respectively. Hillenbrand et al. (1998) show that because of physical effects (disc inclination, inner holes etc) and also observational uncertainties, this threshold is fuzzy and not capable of establishing or excluding accretion in all cases. Unfortunately, mid-IR measurements which are much more sensitive are only available for a small fraction of the sample (see Rebull et al. 2006). An alternative is to use EW[Ca], which goes into emission

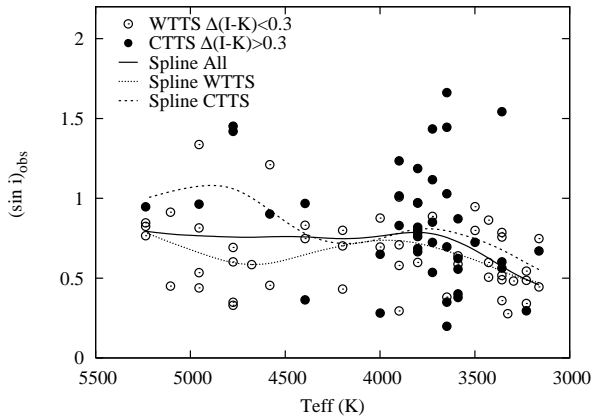


Figure 3. The observed value of $\sin i$ (from equation 1) versus the effective temperature. CTTS/WTTS are indicated by different symbols. The lines show low order spline fits as a function of T_{eff} to (a) all the data, (b) the CTTS only ($\Delta(I - K) > 0.3$), (c) the WTTS ($\Delta(I - K) < 0.3$).

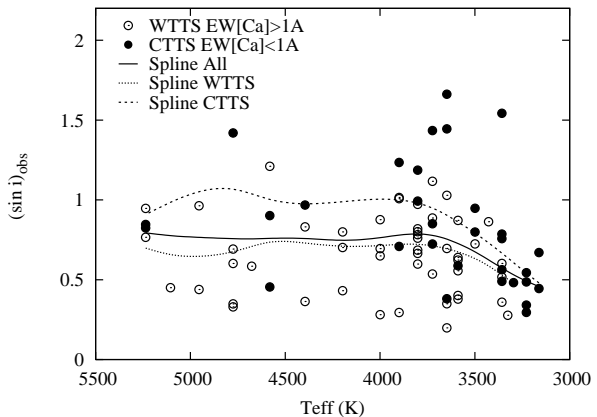


Figure 4. Similar to Fig. 3, but here the WTTS and CTTS are classified according to whether the equivalent width of the Ca II 8542 Å line is more or less than 1 Å (see Hillenbrand et al. 1998).

for strongly accreting objects. WTTS are generally found to have $\text{EW}[\text{Ca}] > 1 \text{ Å}$ and Fig. 4 repeats Fig. 3 using this criteria to separate WTTS and CTTS. Although crude, these diagnostics should be sufficient to identify cases where broad-band colours, magnitudes and hence estimated luminosities and radii are likely to be affected, which is the issue here.

Two sample selection issues are highlighted by Figs. 3 and 4. The first is that stars with a near infrared excess or $\text{EW}[\text{Ca}] < 1 \text{ Å}$ have a larger $(\sin i)_{\text{obs}}$ on average than those without. To illustrate this, smooth spline fits as a function of T_{eff} are plotted for all the data and for the CTTS/WTTS subsets separately. The effect is small at cool temperatures but increases to ≈ 30 per cent in hotter stars. For stars with $T_{\text{eff}} > 3499 \text{ K}$ (see below) the average $\sin i$ is 0.78 ± 0.04 , but the averages for the WTTS samples are 0.69 ± 0.04 for 34 stars with $\Delta(I - K) < 0.3$ and 0.67 ± 0.04 for 44 stars with $\text{EW}[\text{Ca}] > 1 \text{ Å}$. As the estimated distance is linearly dependent on $(\sin i)_{\text{obs}}$, this bias is of concern. There are no physical reasons to suppose that CTTS have larger inclination angles, but there are good reasons to suppose that the

radii of CTTS have been underestimated (leading to a $\sin i$ overestimate), either because of a systematic underestimation of the extinction and luminosity (see Hillenbrand 1997) or because of difficulties in determining their temperatures (see below and section 6).

The second issue is that the average $(\sin i)_{\text{obs}}$ appears to get smaller for $T_{\text{eff}} < 3499$ K (corresponding to spectral types cooler than M2) in both WTTS and CTTS. The average $(\sin i)_{\text{obs}}$ for WTTS ($\Delta(I-K) < 0.3$) with $T_{\text{eff}} < 3499$ K falls to only 0.53 ± 0.04 . There are a number of possible causes for this. (i) Perhaps the binary fraction is a strong function of mass (and therefore T_{eff}). A larger binary fraction, or tendency towards high q systems will increase the average R_{obs} and hence reduce the average $(\sin i)_{\text{obs}}$. The evidence from field stars is that the binary fraction falls significantly towards lower masses, so this explanation seems unlikely. (ii) The observed radius is derived from L and a T_{eff} which is derived from the Cohen & Kuhi (1979) main-sequence relationship between T_{eff} and spectral type. For warmer stars ($T_{\text{eff}} \geq 3500$ K) this relationship is relatively uncontroversial in the sense that alternative scales (for instance Kenyon & Hartmann 1995; Leggett et al. 1996) differ by less than 2 per cent and not in a systematic way. For cooler stars the relationship is more uncertain and especially so for very cool PMS stars which have significantly lower gravities than main-sequence stars of similar spectral type. The luminosity estimates are also reliant on an accurate assessment of the extinction which requires intrinsic broadband colours for very cool PMS stars. Hillenbrand (1997) used the intrinsic colours of main-sequence stars tabulated by Bessell & Brett (1988), but very cool PMS stars may have more giant-like colours. Dwarfs are bluer than giants by ~ 0.3 mag in $V-I$ for spectral types M3-M5, which would lead to a larger extinction estimate by ~ 0.5 mag (at I). This gives a larger luminosity estimate by 0.2 dex, a larger radius estimate by 0.1 dex and hence a decreased $\sin i$ estimate by a factor of 1.26 that would almost entirely explain the trend seen.

For the reasons above the analysis here is initially restricted to the $\sin i$ distribution of those 34 objects in Table 1 with $\Delta(I-K) < 0.3$ and $T_{\text{eff}} > 3499$ K. This sample is labelled WTTS1 in what follows. Two alternate samples are also considered, namely 44 objects with $T_{\text{eff}} > 3499$ K and $\text{EW}[\text{Ca}] > 1\text{\AA}$ (labelled WTTS2) and all 74 objects with $T_{\text{eff}} > 3499$ K, regardless of their accretion status (labelled ALL).

5.2 The v_{true} distribution

For the reasons explained in section 4.2, a reasonable model of the v_{true} distribution is required and can be constrained by comparing the simulated $v \sin i$ distribution (from many trials) with that observed.

In Figure 5 two of these comparisons are shown. A formal statistical comparison has been made using a 1-dimensional K-S test of the CDFs. The models shown have $i_{\text{th}} = 30^\circ$, but the model $v \sin i$ distribution does not depend strongly on this parameter.

After experimenting with a variety of simple analytical forms, I find that a two component v_{true} model (labelled v1 in Fig. 5) provides a good (though not necessarily unique) fit to the data, with 80 per cent of stars

following an exponentially decaying distribution between $10 < v_{\text{true}} < 120 \text{ km s}^{-1}$, with a decay constant of 20 km s^{-1} , and the remaining 20 per cent being uniformly distributed between $10 < v_{\text{true}} < 120 \text{ km s}^{-1}$. The K-S test indicates a probability of 85 per cent for the null hypothesis that the data is drawn from the model distribution. On the other hand, the K-S test shows that a flat v_{true} distribution (labelled v2 in Fig. 5) can be excluded with 99.999 per cent confidence.

5.3 Distance estimates

Following the procedure in section 4.4, the distributions of α and $(\sin i)_{\text{obs}}$ were calculated and used to estimate the cluster distance from equation 8. A K-S test comparison was performed between the CDFs of $\alpha(D/470)$ and $(\sin i)_{\text{obs}}$ to test whether the model is a reasonable representation of the data. Statistical uncertainties were estimated by generating fake datasets of the same size, with v_{true} and binary properties drawn from the distributions used in each model. Observational errors for the fake datasets matched those in the real dataset considered here. The fake datasets passed through the same analysis procedure and the standard deviations of the distance estimates (from 300 fake datasets) were used as estimates of the statistical error.

The results are collected in Table 2, and Fig. 6 demonstrates the sensitivity of the model distribution to changes in the various parameters in the form of both the differential and cumulative distributions of $\alpha(D/470)$ compared with those of the data.

Analysis number 1 from Table 5 is used as a baseline for the discussion as this uses the parameters that could be considered to most likely represent the modelled ONC population. The average value of $(\sin i)_{\text{obs}}$ is significantly lower than would be expected for randomly inclined axes in agreement with the analysis of Rhode et al. (2001) based on a smaller sample. The simplest explanation is that the ONC is much closer than the 470 pc assumed by Hillenbrand (1997). Indeed $D = 470$ pc is rejected with 97 per cent confidence. I find a distance of 392 pc gives a much better representation of the data as may be judged from Figs. 6a and 6b. The statistical uncertainty is ± 23 pc which compares well with simulations and uncertainty estimates presented by O'Dell et al. (1993) for similar sized samples.

In addition to the statistical uncertainties I have tried other models to test the sensitivity of the derived distance to variations in model parameters that are only partially constrained. Fig. 6 shows examples of the model distributions at a fixed distance of 392 pc in order to highlight these differences. The reader should note that in all cases the variations in the intrinsic α distribution can be compensated for by changes in the cluster distance to yield a reasonable value for $P(\text{K-S})$ (these are the results quoted in Table 2). Therefore the observed $(\sin i)_{\text{obs}}$ distribution is currently incapable of constraining some of the more interesting parameters like i_{th} , due to the small sample size and experimental errors.

Figs. 6c and 6d show how changes of $15^\circ < i_{\text{th}} < 45^\circ$ affect the modelled distribution at a fixed distance of 392 pc. The changes are small and easily compensated for by modest changes in the cluster distance of only ± 4.0 per cent. This range seems a reasonable estimate of the uncertainties engendered by the inclination bias – if $i_{\text{th}} < 15^\circ$ this would

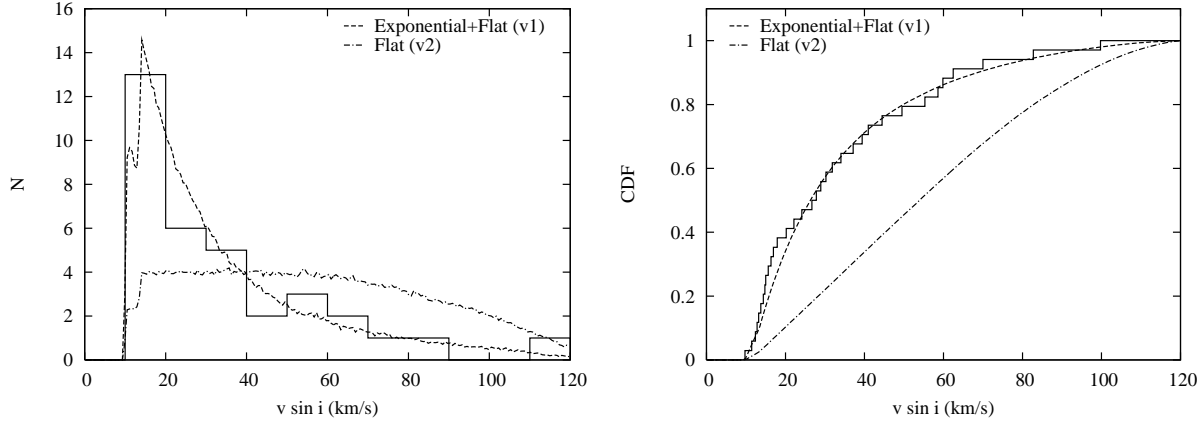


Figure 5. A comparison of the observed $v \sin i$ distribution with Monte-Carlo simulations based on two different models of the v_{true} distributions, v1 and v2 (described in the text). The left panel shows the (binned) distributions and the right panel shows the normalised cumulative distributions used to perform a Kolmogorov-Smirnov test. The discontinuity in the model distributions at $v \sin i = 13.6 \text{ km s}^{-1}$ is due to the modelled sample being divided between objects with detectable $v \sin i$ thresholds at 13.6 km s^{-1} and 10 km s^{-1} .

Table 2. The results of the distance analysis. The columns are: (1) An analysis identification number; (2) the analysed sample and number of objects in the sample – WTTS1 indicates objects $\Delta(I - K) < 0.3$, WTTS2 indicates objects $\text{EW}[\text{Ca}] > 1 \text{ \AA}$ (see section 5.1), ALL indicates no $\Delta(I - K)$ restriction; (3) identifies which $\Delta R(q)$ model was used, r1 or r2 (see section 4.3); (4) identifies which v_{true} distribution was assumed, v1 or v2 (see section 5.2); (5) the assumed value of i_{th} (see section 3.2); (6) the assumed value of the binary fraction f (see section 4.3); (7) the assumed value of uncertainty in the observed (log) radius (see section 3.1); (8) the average value of $\langle \sin i \rangle_{\text{obs}}$; (9) the average value of α ; (10) the distance implied by equation 8 and its 1-sigma statistical uncertainty; (11) the Kolmogorov-Smirnov null-hypothesis probability (the probability that the observed distribution is not drawn from the model distribution is $1 - P(K-S)$).

Analysis No.	Sample (n)	$\Delta R(q)$ model	v_{true} model	i_{th} degrees	bfrac f	$\delta_{\log R}$ (dex)	$\langle (\sin i)_{\text{obs}} \rangle$	$\langle \alpha \rangle$	D (pc)	$P(K-S)$
1	WTTS1 (34)	r1	v1	30	0.5	0.11	0.691	0.828	392 ± 23	0.66
2	WTTS1 (34)	r1	v1	15	0.5	0.11	0.691	0.802	405 ± 24	0.75
3	WTTS1 (34)	r1	v1	45	0.5	0.11	0.691	0.870	373 ± 22	0.61
4	WTTS1 (34)	r1	v1	30	0.3	0.11	0.691	0.858	378 ± 22	0.67
5	WTTS1 (34)	r1	v1	30	0.7	0.11	0.691	0.798	407 ± 24	0.63
6	WTTS1 (34)	r1	v1	30	0.5	0.07	0.691	0.812	400 ± 18	0.64
7	WTTS1 (34)	r1	v1	30	0.5	0.15	0.691	0.851	382 ± 28	0.41
8	WTTS1 (34)	r1	v2	30	0.5	0.11	0.691	0.815	398 ± 24	0.64
9	WTTS1 (34)	r2	v1	30	0.5	0.11	0.691	0.849	383 ± 22	0.68
10	WTTS2 (44)	r1	v1	30	0.5	0.11	0.671	0.829	381 ± 20	0.66
11	ALL (74)	r1	v1	30	0.5	0.11	0.780	0.834	440 ± 19	0.48

make little further difference to the distance estimate and if $i_{\text{th}} > 45^\circ$ then there would be difficulties in measuring rotation periods in a large fraction of WTTS.

Figs. 6e and 6f show the effects of changing the binary frequency between $0.3 < f < 0.7$ at a fixed distance. Again the small differences can be compensated for by small changes (± 3.7 per cent) in distance – larger f leads to larger distances.

Figs. 6g and 6h show that changing the assumed value of $\delta_{\log R}$ in the plausible range $0.07 < \delta_{\log R} < 0.15$ significantly changes the shape of the distribution at a fixed distance. This can be partially compensated for by changing the distance by ± 2.3 per cent. The broader distribution is a poorer fit to the cumulative distribution function but cannot be rejected.

Figs. 6i and 6j show that even taking implausibly large variations in the v_{true} and $\Delta R(q)$ distributions (see sections 5.2 and 4.3 respectively) results in very small changes

in the model that can be compensated for by changes in the cluster distance of only ± 1.9 per cent.

For completeness, I show the effects of considering the sample of 74 objects (ALL) including both CTTS and WTTS (but all with spectral types of M2 or hotter) and also a sample of WTTS defined on the basis of $\text{EW}[\text{Ca}]$ (WTTS2 – see section 5.1). As expected from Figs. 3 and 4 and the discussion in section 5.1 the distribution for the entire sample is skewed to higher $\langle \sin i \rangle_{\text{obs}}$ values, resulting in a significantly larger distance estimate with slightly better statistical precision (440 ± 19 pc). The sample of WTTS based on $\text{EW}[\text{Ca}]$ is larger than sample WTTS1 but filters out a few more of the objects with large $\langle \sin i \rangle_{\text{obs}}$ values. Hence the deduced distance based on sample WTTS2 is marginally closer than that based on sample WTTS1.

The “best” final ONC distance estimate is 392 pc. The total uncertainty is 32 pc, estimated from quadratic sum of the statistical uncertainty and the distance uncertainties due

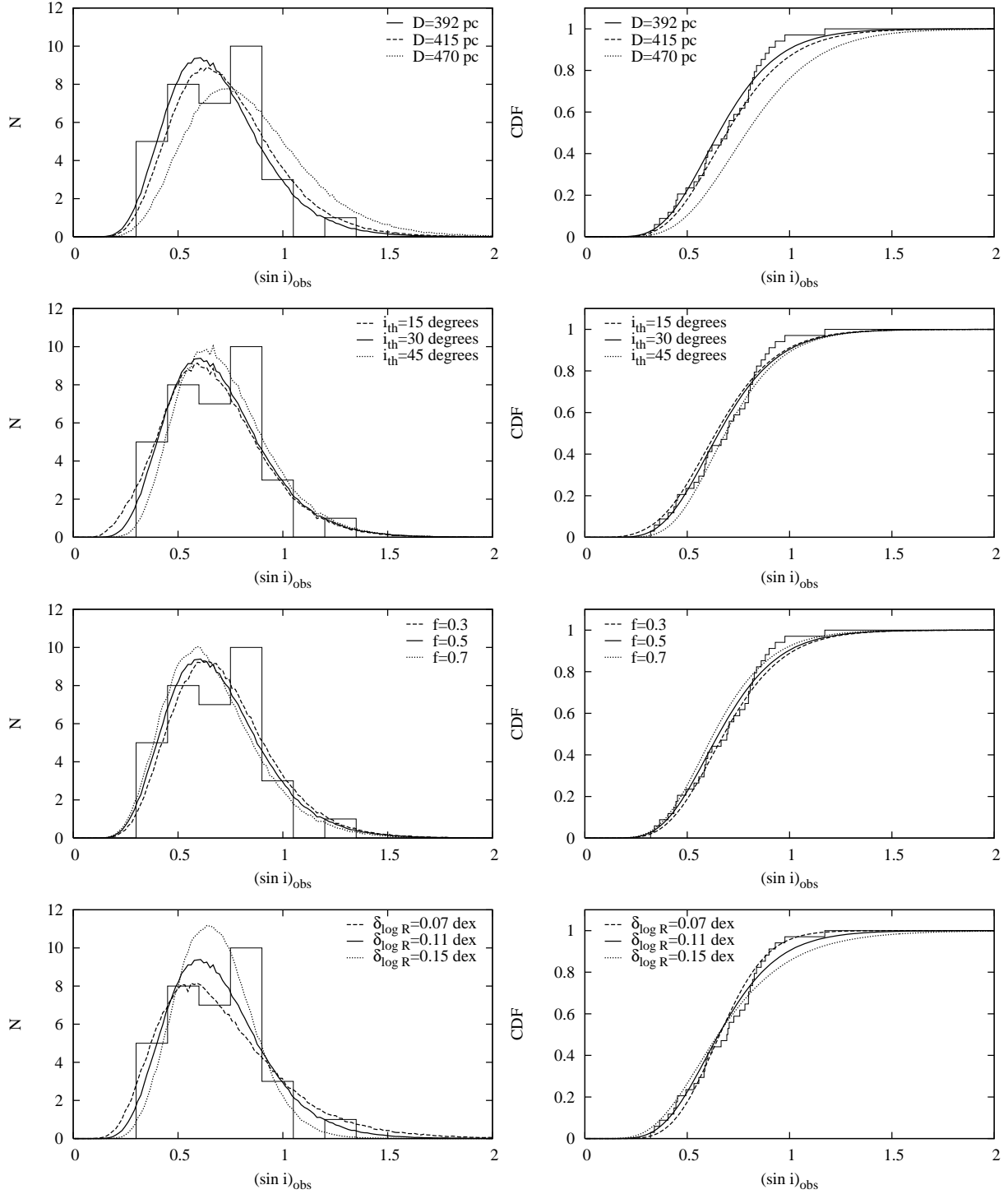


Figure 6. The observed $(\sin i)_{\text{obs}}$ distribution compared with various model distributions of the form $\alpha(D/470 \text{ pc})$. The left hand panels show the differential distributions while the right hand panels show the normalised cumulative distributions. (a, b) Shows the effects of distance on the data-model comparison. The three models shown corresponds to model 1 in Table 5 at $D = 392$ pc, model 1 at $D = 415$ pc (corresponding to a 1-sigma error) and model 1 at $D = 470$ pc. (c, d) Shows the effects of varying i_{th} by displaying models 1, 2 and 3 ($i_{\text{th}} = 30^\circ, 15^\circ$ and 45°) at a common $D = 392$ pc. (e, f) Shows the effects of varying the binary fraction f by displaying models 1, 4 and 5 ($f = 0.5, 0.3$ and 0.7) at a common $D = 392$ pc. (g, h) Shows the effects of varying $\delta_{\log R}$ by displaying models 1, 6 and 7 ($\delta_{\log R} = 0.11$ dex, 0.07 dex and 0.15 dex) at a common $D = 392$ pc.

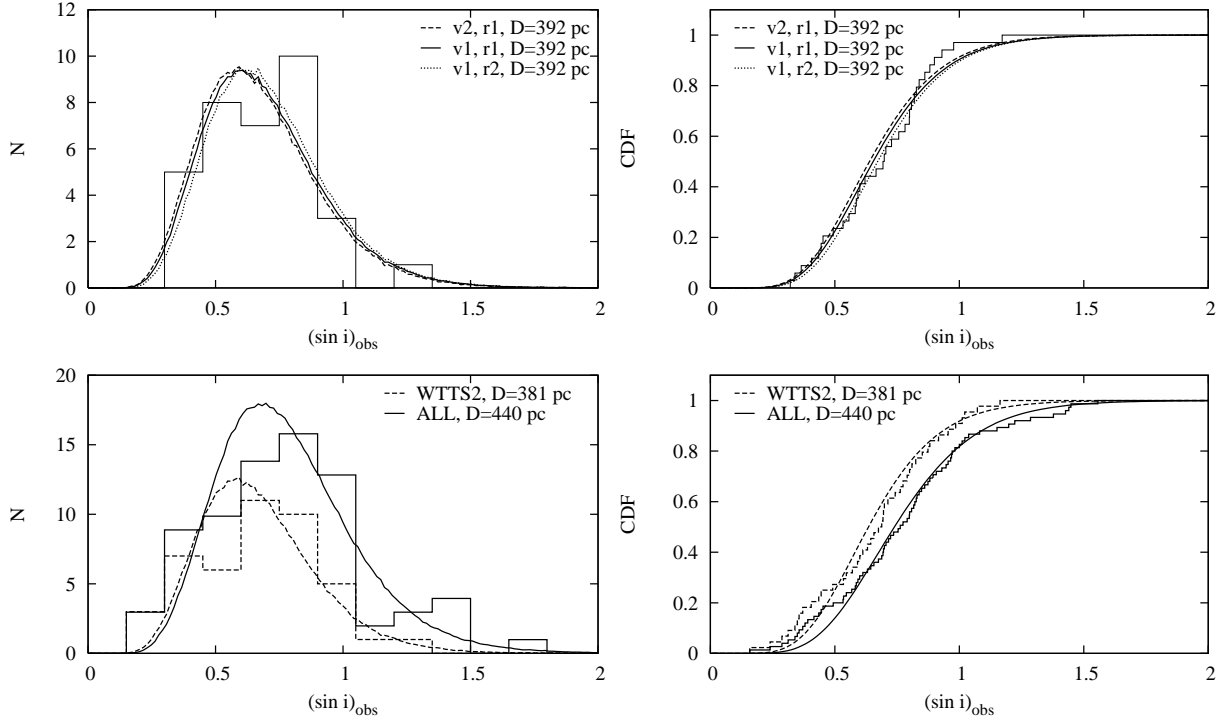


Figure 5. continued: (i, j) Shows the effects of choosing different v_{true} (v_1 , v_2) and $\Delta R(q)$ (r_1 , r_2) distributions by displaying models 1, 8 and 9 at a common $D = 392$ pc. (k, l) Shows a model which best fits a sample of WTTs defined using EW[Ca] (see section 5.1) (model 10 at $D = 381$ pc) and a model which best fits a sample containing both CTTS and WTTs (model 11 at $D = 440$ pc).

to the parameter variations discussed above. This of course assumes these uncertainties are independent, ignores any systematic problem with the spectral type-effective temperature relationship, and assumes that it is correct to exclude CTTS from the analysis. The equivalent figure including the CTTS would be 440 ± 34 pc, where the uncertainty in this case is dominated by systematic effects.

6 DISCUSSION AND CONCLUSIONS

The observed $\sin i$ distribution of a group of WTTs (and CTTS) in the ONC has been modelled. The $\sin i$ values are linearly dependent on the cluster distance and from this a distance to the ONC of 392 ± 32 pc is derived or 440 ± 34 pc if CTTS are included in the sample. The uncertainties include 1-sigma statistical uncertainties and the contributions from uncertainties in a number of other partially constrained model parameters such as the binary frequency, bias against the inclusion of low inclination objects, the form of the true equatorial velocity distribution and uncertainties in the stellar radius estimates. With the present analysis and observational sample (34 WTTs), statistical and systematic uncertainties are of equal importance.

The observed $\sin i$ values depend linearly on the estimated radii, which are difficult to determine for PMS stars. Hillenbrand (1997) discusses these difficulties and concluded that extinctions, luminosities and hence radii may be underestimated for accreting CTTS, resulting in overestimates of $\sin i$ and hence overestimates of the distance using the analysis presented in this paper. This effect is readily apparent in the data, even when using imperfect discriminators of ac-

cretion activity such as the $I - K$ excess and EW of the Ca II 8542Å line. A more careful analysis could use mid-IR measurements to exclude (accretion) discs, but for now it seems wisest to discard the suspected CTTS and adopt the closer of the two distance estimates above.

A further issue is the validity of the spectral-type/effective temperature relationship. As stated in section 5.1, the relationship of Cohen & Kuhi (1979) is uncontroversial in that it is consistent with several later studies. However, these are also fundamentally based on the atmospheres, angular diameters and bolometric luminosities of cool main sequence stars. Young PMS stars are likely to have different atmospheres and the fact that rotational modulation has been measured in our sample stars means that they must be covered by cool spotted regions. Assigning a single temperature to such magnetically active stars may be difficult. These difficulties could be worse in CTTS with their attendant discs, veiling and accretion hotspots and this is a further reason for excluding them from the analysis. As yet, there is no compelling evidence for a change in the spectral-type/temperature relationship for non-accreting PMS stars, but as deduced distances will scale as T_{eff}^2 this issue should be borne in mind.

The deduced ONC distance is smaller than most previous results, although generally agrees within the error bars. If proper account of systematic uncertainties is included, the distance derived here is also probably more accurate than most previous determinations. It is worth noting however the excellent agreement with the 419 ± 21 pc determined by Stassun et al (2004) from an eclipsing binary that they considered to be a possible ONC member.

To recover the more usually used longer ONC distance

of 450 pc or 470 pc (e.g. Hillenbrand 1997; Preibisch et al. 2005) from the rotational data would require a model with a very high binary fraction ($f \simeq 1$) combined with a several per cent change in the relationship between spectral type and temperature for warm K–M2 ONC stars. A closer distance reduces deduced luminosities in the ONC by a corresponding factor. Perhaps more importantly, ages deduced from the positions of PMS stars in the HR diagram are increased by a factor of $\simeq 1.7$, because $L \propto t^{-2/3}$ on fully convective PMS tracks.

The distance determined here is independent of stellar evolutionary models – an important source of systematic error in HR diagram-based estimates. However, it does hinge on the assumption that the rotation axes of PMS stars are randomly oriented in space. The observed $\sin i$ distribution is certainly consistent with this hypothesis, but is also sufficiently broadened by experimental uncertainties that other hypotheses cannot be rejected. For example, taking the parameters of model 1 in Table 2 and using a fixed inclination $i = 60^\circ$ results in a distance of 396 pc and $P(K-S) = 0.48$.

The theoretical and observational justification for random axial orientation is mixed. In the quasi-static picture of star formation, cloud collapse occurs preferentially parallel to magnetic field lines. Some polarization studies suggest that disc (and therefore presumably rotation) axes could be aligned with the large scale magnetic fields in star forming regions (e.g. Vink et al. 2005). On the other hand, imaging of CTTS discs in the Taurus-Auriga region reveals a random orientation with respect to the large scale magnetic field, in accord with a more dynamical star formation picture (Ménard & Duchêne 2004).

As a final remark, previous applications of the rotationally based technique to the Pleiades cluster and Taurus-Auriga association have yielded distances which turn out to be in good agreement with later precise parallax-based measurements (see O'Dell et al. 1994; Preibisch & Smith 1997). This tends to argue that the underlying assumptions of the method (random axial orientations and a dwarf-like temperature scale for non-accreting PMS stars) are reasonable. A subsequent precise trigonometric parallax for the ONC (e.g. using the Hubble Space Telescope) could be used to test the robustness of these model assumptions in more detail.

7 ACKNOWLEDGEMENTS

I thank William Herbst for some very useful comments on the initial version of this paper.

REFERENCES

- Anthony-Twarog B. J., 1982, *AJ*, 87, 1213
 Baraffe I., Chabrier G., Allard F., Hauschildt P. H., 2002, *A&A*, 382, 563
 Bertout C., Robichon N., Arenou F., 1999, *A&A*, 352, 574
 Bessell M. S., Brett J. M., 1988, *PASP*, 100, 1134
 Breger M., Gehrz R. D., Hackwell J. A., 1981, *ApJ*, 248, 963
 Cohen M., Kuhl L. V., 1979, *ApJS*, 41, 743
 Duquennoy A., Mayor M., 1991, *A&A*, 248, 485
 Fischer D. A., Marcy G. W., 1992, *ApJ*, 396, 178
 Genzel R., Reid M. J., Moran J. M., Downes D., 1981, *ApJ*, 244, 884
 Hendry M. A., O'dell M. A., Collier-Cameron A., 1993, *MNRAS*, 265, 983
 Herbst W., Bailer-Jones C. A. L., Mundt R., Meisenheimer K., Wackermann R., 2002, *A&A*, 396, 513
 Herbst W., Mundt R., 2005, *Astrophys. J.*, 633, 967
 Herbst W., Rhode K. L., Hillenbrand L. A., Curran G., 2000, *Astron. J.*, 119, 261
 Hillenbrand L. A., 1997, *AJ*, 113, 1733
 Hillenbrand L. A., Strom S. E., Calvet N., Merrill K. M., Gatley I., Makidon R. B., Meyer M. R., Skrutskie M. F., 1998, *Astron. J.*, 116, 1816
 Huff E. M., Stahler S. W., 2006, *ApJ*, 644, 355
 Johns-Krull C. M., Hatzes A. P., 1997, *ApJ*, 487, 896
 Joncour I., Bertout C., Bouvier J., 1994, *A&A*, 291, L19
 Jones B. F., Walker M. F., 1988, *AJ*, 95, 1755
 Kenyon S. J., Hartmann L. W., 1995, *ApJS*, 101, 117
 Köhler R., Petr-Gotzens M. G., McCaughrean M. J., Bouvier J., Duchêne G., Quirrenbach A., Zinnecker H., 2006, *A&A*, 458, 461
 Lada C. J., Muench A. A., Haisch Jr. K. E., Lada E. A., Alves J. F., Tollestrup E. V., Willner S. P., 2000, *AJ*, 120, 3162
 Leggett S. K., Allard F., Berriman G., Dahn C. C., Hauschildt P. H., 1996, *ApJS*, 104, 117
 Ménard F., Duchêne G., 2004, *A&A*, 425, 973
 Muench A. A., Lada E. A., Lada C. J., Alves J., 2002, *ApJ*, 573, 366
 Neuhäuser R., Wolk S. J., Torres G., Preibisch T., Stout-Batalha N. M., Hatzes A. P., Frink S., Wichmann R., Covino E., Alcalá J. M., Brandner W., Walter F. M., Sterzik M. F., Koehler R., 1998, *A&A*, 334, 873
 O'Dell C. R., 1998, *AJ*, 115, 263
 O'Dell M. A., Hendry M. A., Collier Cameron A., 1994, *MNRAS*, 268, 181
 Padgett D. L., Strom S. E., Ghez A., 1997, *ApJ*, 477, 705
 Penston M. V., Hunter J. K., O'Neill A., 1975, *MNRAS*, 171, 219
 Petr M. G., Coude Du Foresto V., Beckwith S. V. W., Richichi A., McCaughrean M. J., 1998, *Astrophys. J.*, 500, 825
 Preibisch T., Smith M. D., 1997, *A&A*, 322, 825
 Prosser C. F., Stauffer J. R., Hartmann L., Soderblom D. R., Jones B. F., Werner M. W., McCaughrean M. J., 1994, *ApJ*, 421, 517
 Rebull L. M., Stauffer J. R., Megeath S. T., Hora J. L., Hartmann L., 2006, *ApJ*, 646, 297
 Rhode K. L., Herbst W., Mathieu R. D., 2001, *AJ*, 122, 3258
 Schüssler M., Caligari P., Ferriz-Mas A., Solanki S. K., Stix M., 1996, *A&A*, 314, 503
 Shuping R. Y., Kassis M., Morris M., Smith N., Bally J., 2006, *ApJ*, 644, L71
 Sicilia-Aguilar A., Hartmann L. W., Hernández J., Briceño C., Calvet N., 2005, *AJ*, 130, 188
 Siess L., Dufour E., Forestini M., 2000, *A&A*, 358, 593
 Simon M., Close L. M., Beck T. L., 1999, *Astron. J.*, 117, 1375
 Slesnick C. L., Hillenbrand L. A., Carpenter J. M., 2004, *ApJ*, 610, 1045
 Stassun K., Mathieu R., 2006, in *American Astronomi-*

- cal Society Meeting Abstracts A Survey For Pre-main-sequence Spectroscopic Binary Stars In The Orion Nebula Cluster. p. 08.03
- Stassun K. G., Mathieu R. D., Mazeh T., Vrba F. J., 1999, *AJ*, 117, 2941
- Stassun K. G., Mathieu R. D., Vaz L. P. R., Stroud N., Vrba F. J., 2004, *ApJS*, 151, 357
- Vink J. S., Drew J. E., Harries T. J., Oudmaijer R. D., Unruh Y., 2005, *MNRAS*, 359, 1049
- Walker M. F., 1969, *ApJ*, 155, 447
- Warren Jr. W. H., Hesser J. E., 1978, *ApJS*, 36, 497

This paper has been typeset from a $\mathrm{T}_{\mathrm{E}}\mathrm{X}/\mathrm{L}^{\mathrm{A}}\mathrm{T}_{\mathrm{E}}\mathrm{X}$ file prepared by the author.